Nanostructured Mo$_3$Al-based composites strengthened by Al$_2$O$_3$ precipitates

A. Sakly[a], J. Costa[b], B. Trindade[b,*], J.V. Fernandes[b], T. Benameur[a]

[a] ENIM, Mechanical Engineering Laboratory, Ave. Ibn El Jazzar, Monastir 5019, Tunisia
[b] CEMUC, Department of Mechanical Engineering, University of Coimbra, Rua Luís Reis Santos, 3030-788, Coimbra, Portugal

ARTICLE INFO

ABSTRACT

Nanostructured Mo$_3$Al-based composites strengthened by Al$_2$O$_3$ precipitates were obtained from a Mo$_{75}$Al$_{25}$ (at.%) + 15 vol.% Al$_2$O$_3$ mixture that was synthesized by mechanical alloying (MA) from Mo, Al and Al$_2$O$_3$ powders and subsequently annealed. The influence of rotation speed and milling time on the structure and mechanical properties of the final compacts, before and after annealing, was studied. After milling at 150 and 300 rpm, mainly a metastable BCC-Mo(Al) solid solution was observed. With subsequent annealing at 900 °C this solid solution decomposed into Mo + Mo$_3$Al (an intermetallic phase). The mechanical properties of the samples mechanically alloyed at 300 rpm are in general better than the ones of samples alloyed at 150 rpm. Values of H = 18.4 GPa, σ_y = 6.2 MPa and E = 227 GPa were obtained from the 300 rpm samples, after annealing at 900 °C. The work-hardening coefficient value, n, obtained from the annealed sample milled at 150 rpm is higher than the one from the as-milled sample (0.05 in contrast to 0.02, respectively), indicating a slight increase in ductility. For 300 rpm no significant variation of n was apparent after annealing (n was about 0.02).

© 2010 Elsevier B.V. All rights reserved.

1. Introduction

Nanostructured intermetallic phases have excellent mechanical and physical properties, such as high hardness and Young's modulus, good corrosion resistance and very high intrinsic strength, particularly at high temperatures. However, these materials cannot be fully exploited for engineering applications due to their extreme brittleness [1]. One strategic way to overcome this problem is to raise the fracture-toughness of these materials by crack bridging with ductile elements, for example pure metals [2,3]. Metal reinforced materials intended for high temperature applications have interesting mechanical properties when designed as interpenetrating networks [4]. However, conventional techniques used for their production are sometimes costly and do not lead to final products with the required mechanical properties.

In this study, a nanostructured Mo$_3$Al–Mo–Al$_2$O$_3$ composite was synthesized by mechanical alloying from Mo, Al and Al$_2$O$_3$ powders. Mechanical alloying, as a powder processing method, induces discontinuous second phases in the intermetallic matrix giving rise to materials with unique microstructures and mechanical properties [5]. Molybdenum and its alloys and compounds have good mechanical properties at high temperatures [6]. Its presence in the matrix can increase the fracture-toughness of the intermetallic-based material [7]. Al$_2$O$_3$ particle reinforcement has

been used in different intermetallic-base systems [8,9], with a consequent density decrease of the composite, improving the creep and wear resistance and increasing mechanical properties such as hardness, tensile strength and Young's modulus [10].

In this investigation, the influence of the milling conditions and annealing temperature on the structure and mechanical properties of the final Mo$_3$Al–Mo–Al$_2$O$_3$ compacts was studied. The processing method combines mechanical alloying of powdered raw materials and subsequent sintering. During mechanical alloying and the subsequent sintering process the presence of Al was expected to reduce molybdenum oxide at the Mo powder surface, in order to form additional Al$_2$O$_3$ ceramic precipitates [11]. Moreover, the reduced metal M reacts with the remaining Al to form intermetallic compounds (M$_y$Al). Consequently, the resultant composition and microstructures can be controlled in order to obtain the desired final properties. The mechanical properties of the synthesised composites were determined by depth-sensing indentation (DSI) [12]. In order to predict the stress–strain behaviour, a reverse analysis methodology using indentation data was performed. This methodology allows the mechanical properties of small volumes to be determined, which is one of the current challenges in material science.

2. Experimental details

A Mo$_{75}$Al$_{25}$ (at.%) + 15 vol.% Al$_2$O$_3$ mixture was synthesized by mechanical alloying from Mo, Al and Al$_2$O$_3$ powders in order to obtain the final chemical composition: Mo$_{85.45}$Al$_{11.51}$O$_{4.14}$ (wt.%) (Mo$_{58.84}$Al$_{28.21}$O$_{12.95}$ (at.%)). The characteristics of the raw materials given by the manufacturer were the following: 99.9% pure Mo obtained
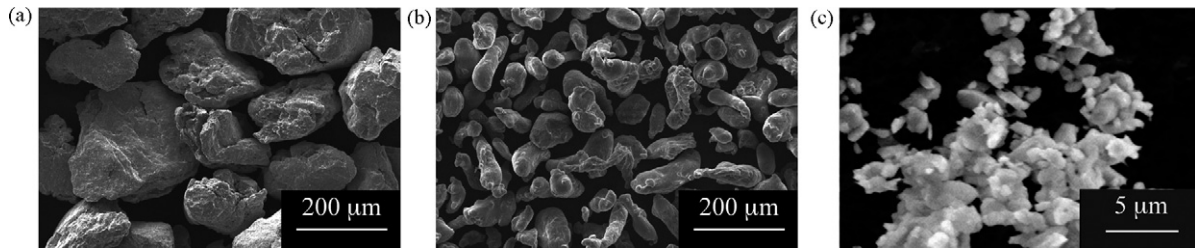
Fig. 1. SEM images of the initial powders: (a) Mo, (b) Al, (c) Al_2O_3.

from Goodfellow with particle sizes in the range of 55–355 μm; 99.5% pure Al obtained from CERAC with particle sizes in the range of 45–74 μm; and 99.9% pure Al_3O_2 obtained from Goodfellow with a mean particle size of 1.8 μm.

Mechanical alloying of this mixture was performed in a planetary ball mill (Pulverisete 6 from Fritsch) for a maximum time of 100 h, using a hardened steel vial and 15 balls with 20 mm diameter. The milling procedure was interrupted every 15 min, for 10 min, to cool down the system. A ball-to-powder weight ratio of 20:1 was used and the milling intensity was adjusted to two different rotation speeds: 150 and 300 rpm. The presence of hard ceramic Al_2O_3 particles accelerates the fragmentation of the powder mixture and therefore no process control agent (PCA) was used. In order to avoid contamination, milling was performed in a hydrogenated argon atmosphere (5% H_2) and was interrupted at selected times to take out small amounts of powder for analysis. Structural analysis using a Philips X'Pert PW3020 X-ray diffractometer with Bragg Brentano geometry was performed. Co-Kα_1 radiation was used (λ = 1.78897 Å). The angular range (2θ) covered was 20–120°, with a step of 0.04° and 1 s of counting time per angle. The identification of the peaks was carried out with reference to the ICDD cards database, using the X'Pert software of the equipment. Particle size distributions were determined by laser scattering (Cilas 1064 equipment) from a powder suspension in water, under mechanical agitation after a 60 s sonication. Thermal stability of the mechanically alloyed mixtures was evaluated by differential scanning calorimetry, using a Setaram-Setsys Evo-1750 apparatus with a heat rate of 40 °C/min and Ar + 5% H_2 atmosphere. A Philips XL30 with EDS microanalysis (EDAX) was used for morphological characterization of the mixtures as well as for chemical composition analysis. A Cameca SX-50 Electron Probe Microanalysis (EPMA) apparatus was also used for this purpose. The mechanically alloyed mixtures were compacted under cold isostatic pressure in a Stansted Fluid Power Ltd. apparatus by applying 220 MPa of pressure for 15 min. Compacts 30–35 mm long and 5–6 mm thick were obtained. The compacts were subsequently annealed in vacuum at different temperatures (600–900 °C). The influence of temperature on the final structure and mechanical properties of the compacts was studied.

Mechanical properties of the milled mixtures, both with and without subsequent annealing, were determined by the depth-sensing indentation technique, using Fischerscope H100 indentation equipment with a Vickers diamond indenter. From the recorded load–indentation depth curve, mechanical properties other than hardness were estimated, such as the Young's modulus and the stress–plastic strain(curve. Reverse analysis was used to determine the stress–plastic strain curves, following the methods described in Refs. [13,14]. In order to have representative average values for the evaluated properties, 10 Vickers indentation tests were performed on each sample. During indentation, the load was applied in steps until a nominal load of 100 mN was reached. Sixty steps were used for loading and 60 for unloading.. The time between consecutive steps was 0.5 s. The first load step was always 0.4 mN; for subsequent steps, the value of the load increment between two consecutive steps,
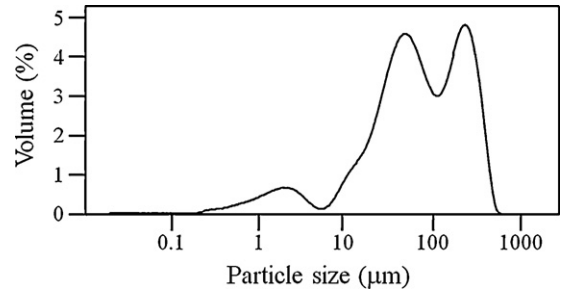

Fig. 2. Particle size distribution of the $Mo_{75}Al_{25}$ + 15 vol.% Al_2O_3 initial mixture.
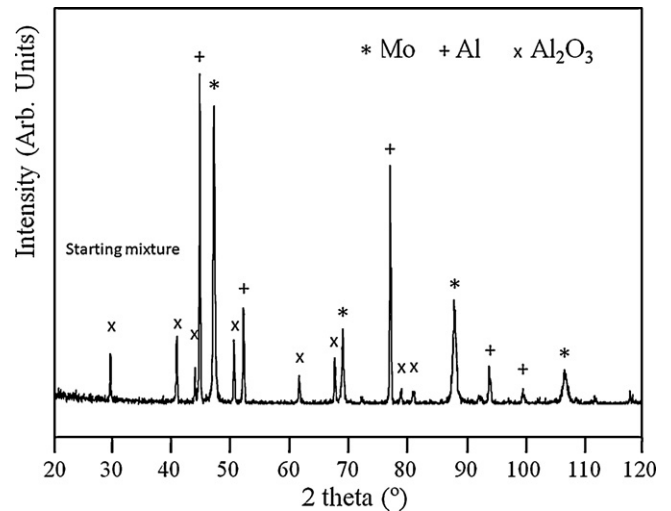

Fig. 3. XRD pattern of the $Mo_{75}Al_{25}$ – 15 vol.% Al_2O_3 powder mixture.
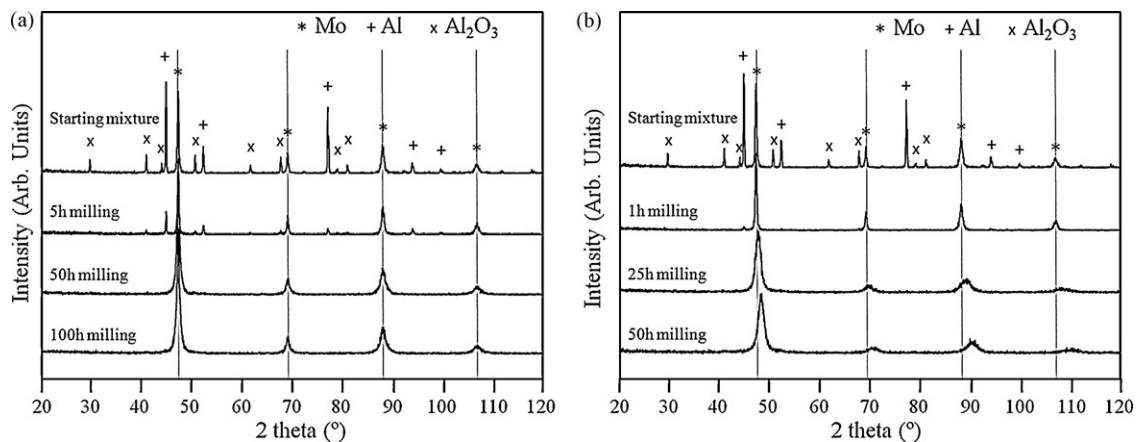

Fig. 4. X-ray diffraction patterns of the powder mixtures for (a) 150 rpm and (b) 300 rpm after different periods of milling time. (Vertical dashed lines correspond to the theoretical BCC-Mo phase diffraction lines).

$\Delta P = P_i - P_{i-1}$, was such that $\sqrt{P_i} - \sqrt{P_{i-1}}$ was constant. Two creep periods of 30 s were programmed during the tests: at maximum load and at the lowest load during unloading (0.4 mN).

3. Results and discussion

3.1. Characterization of the initial powders

The size and morphology of the initial particles were analyzed by SEM (Fig. 1). The particles have different sizes and shapes. As indicated by the suppliers, the biggest particles correspond to Mo whilst the smallest ones are Al_2O_3. The Mo particles have a rounded shape with a rough surface, typical of ductile materials. The Al particles are long and elliptical with a rough surface.

The particle size distribution of the raw $Mo_{75}Al_{25}$ (at.%) + 15 vol.% Al_2O_3 mixture was determined by laser scattering (Fig. 2). The distribution curve confirms the existence of three peaks centered close to 2, 50 and 250 μm, corresponding to the Al_2O_3, Al and Mo particles, respectively.

The XRD pattern of the initial mixture is shown in Fig. 3. Well defined diffraction peaks of the BCC-Mo, FCC-Al and α-Al_2O_3 phases are present, corresponding to long range order crystalline structures.

3.2. Mechanical alloying of $Mo_{75}Al_{25}$ + Al_2O_3 powder mixture

The $Mo_{75}Al_{25}$ (at.%) + 15 vol.% Al_2O_3 powder mixture was mechanically alloyed for a maximum of 100 h. Fig. 4a and b show the XRD patterns of the powder mixtures as a function of rotation speed and milling time. For the alloy synthesized at 150 rpm (Fig. 4a), after 5 h milling, the mixture was still composed of the same structural phases as the raw materials: Mo (BCC), Al (FCC) and α-Al_2O_3. After 50 h, the peaks of the Al-phase were no longer visible, meaning that this element had been incorporated into the BCC-Mo phase in substitutional positions, giving rise to a Mo(Al) solid solution. According to the Mo–Al phase diagram, Al is insoluble in the BCC-Mo phase at room temperature, which means that a Mo(Al) supersaturated solid solution was formed during milling. It is known that mechanical alloying can synthesize a variety of equilibrium and non-equilibrium alloy phases from blended elemental powders or pre-alloyed powders [15,16]. Peaks of α-Al_2O_3 are almost undetectable after 50 h milling, which may be due to the decrease in the crystallinity of this phase and to its lower content in the mixture. A broadening of the Mo diffraction peaks occurred between 5 and 50 h of milling which is attributed to solid solution formation as well as to stresses and defects provoked by milling. Zdujid et al. [17] found that during mechanical alloying of an Al–75 at.% Mo mixture for 1000 h no structural changes were observed between 50 and 100 h of milling. However, a further broadening of the Mo XRD peaks occurred during that period of time. The XRD peaks of the BCC-Mo phase were slightly displaced to higher angles during milling, corresponding to a small decrease in the lattice parameters (Fig. 5). This result is in agreement with the work of Enzo et al. [18] on a mechanically alloyed $Al_{75}Mo_{25}$ (at.%) mixture. According to this author, the incorporation of Al into the BCC-Mo phase does not induce an important variation in the lattice parameter (the values are within the margin of experimental error). However, taking into account the atomic radii of Mo and Al (1.39 and 1.25 Å, respectively), a significant decrease in the BCC lattice parameter should be expected. SEM and elemental chemical analysis of the mixture milled at 150 rpm for 100 h showed some chemical composition heterogeneities (Fig. 6). It is likely that these mechanical synthesis conditions do not produce complete chemical homogeneity in the Mo(Al) solid solution, which means that there will be domains with different chemical compositions and structural range orders. The existence of a BCC Al-rich phase with
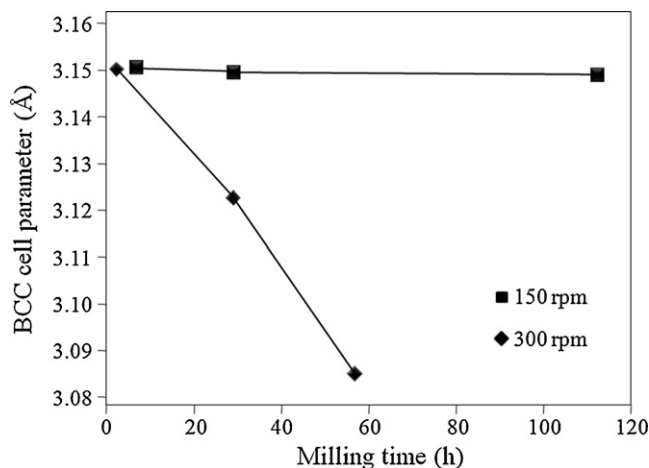

Fig. 5. Variation of a lattice parameter of the Mo solid solution for 150 and 300 rpm as a function of milling time.

a low range order after milling may explain the small variation of the Mo(Al) lattice parameter observed after 100 h of milling.

The structural evolution of the powder mixture synthesized at 300 rpm (Fig. 4b) follows the same trend as the one synthesized at 150 rpm. However, there is a clear displacement of all the XRD peaks of the BCC-Mo solid solution phase to higher angles for long milling times, which corresponds to a significant decrease in the lattice parameter (Fig. 5). The value measured for 300 rpm/50 h of milling is 3.083 Å, which is quite different from that of the equilibrium BCC-Mo phase (3.147 Å). Milling at 300 rpm is a more energetic synthesis process, allowing a higher diffusion mechanism and consequently the formation of a homogeneous single BCC phase after a few hours of processing. In fact, no chemical composition fluctuations were detected after 50 h of milling at 300 rpm.

The crystal size (D) and microstrain of the milled samples were determined from the integral breadth (β) of reflections shown in Fig. 4(a) and (b), using the Halder–Wagner approach [19]:

$$\left(\frac{\beta^*}{d^*}\right)^2 = \frac{1}{D}\frac{\beta^*}{(d^*)^2} + \left(\frac{\varepsilon}{2}\right)^2 \tag{1}$$

where $\beta^* = \beta\cos\theta/\lambda$ and $d^* = d\cos\theta/\lambda$; θ is the Bragg angle and λ is the wavelength used. The plot of $(\beta^*/d^*)^2$ versus $\beta^*/(d^*)^2$ is a straight line, for which the intercept and the slope allow the values of the microstrain (ε) and the crystallite size (D), to be determined.

As expected and illustrated in Table 1, the grain size values decreased as a function of increasing milling time. This was expected for 300 rpm due to the more energetic milling conditions used. The final grain size value obtained for the sample milled
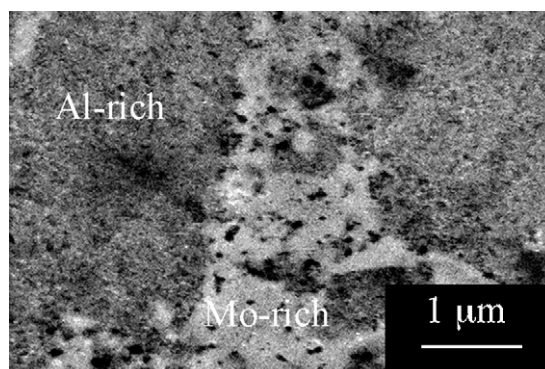

Fig. 6. BSE-SEM image of the 150 rpm/100 h mechanically alloyed mixture.

Table 1
Grain size and microstrain values of the Mo(Al) phase for different milling parameters.

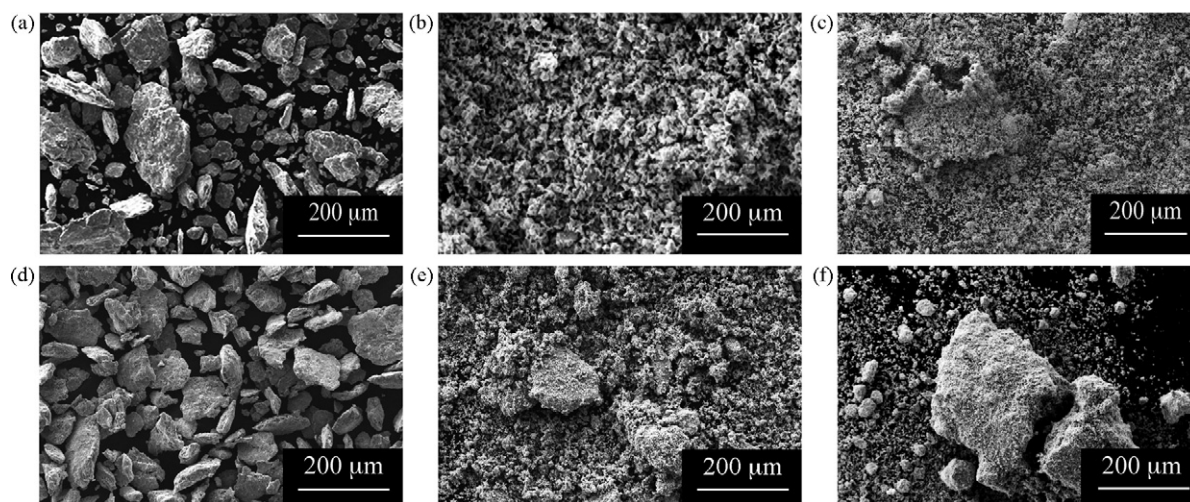| Milling time (h)	150 rpm		300 rpm	
	Grain size (nm)	Microstrains (%)	Grain size (nm)	Microstrains (%)
1	–	–	200	0.49
5	167	0.40	–	–
25	–	–	32	0.90
50	53	0.89	14	1.90
100	33	0.63	–	–

Fig. 7. SEM images of the mechanically alloyed mixtures. (a) 150 rpm/5 h; (b) 150 rpm/50 h; (c) 150 rpm/100 h; (d) 300 rpm/1 h; (e) 300 rpm/25 h; (f) 300 rpm/50 h.

for 100 h at 150 rpm was 33 nm and after 50 h at 300 rpm grain size was 14 nm. Consequently, one might say that after MA both powder mixtures are formed of nanometric Mo(Al) metastable phases. Microstrains arose from distortion of the cubic lattice, which increased with milling time up to 50 h. A decrease in distortion values was however observed from 50 to 100 h milling (150 rpm).

The evolution of particle size as a function of milling time was followed using SEM. Qualitative and quantitative chemical analysis was performed using EDS. Fig. 7 shows the morphology of the particles for the two rotation speeds, after different periods of milling time. For both cases, there is a decrease in particle size with increasing milling time. For the maximum milling time, particle agglomeration can be observed, in particular for 300 rpm. Laser scattering was used for the characterization of the final mechanically alloyed mixtures. The characteristic values obtained from the particle size distributions (the average of the multimodal curves) are shown in Table 2 and confirm the SEM observations. In fact, in both cases, a clear decrease in these characteristic values occurred during milling, in particular for the 300 rpm process.

The $Mo_{75}Al_{25}$ (at.%) + 15 vol.% Al_2O_3 system can be considered as a ductile-brittle system. The microstructural evolution in this type of system has been described by Benjamin [20]. In the initial stages of milling, the ductile Mo and Al powder particles get flattened by the collisions, while the Al_2O_3 becomes fragmented and gets trapped in the ductile particles. With increasing MA time,

the composite powder particles become work hardened, the hardness and consequently the brittleness increases, and the particles become fragmented. A decrease in particle size occurs at this stage. Finally, the hardness and particle size tend to reach a saturation value, called the steady-state processing stage.

Quantitative analysis performed by electron probe microanalysis from the Mo-Lα, Al-Kα, O-Kα and Fe-Kα lines give rise to the results presented in Table 3. The same Mo/Al wt.% ratio was obtained for both mixtures after MA. The Fe value obtained for the mixture mechanically alloyed at 300 rpm for 100 h is excessively high, meaning that there was a significant level of contamination from the grinding media (vial and balls) during processing under these conditions.

3.3. Thermal stability of the mechanically alloyed mixtures

Taking into account that these materials are to be used at high temperatures, their thermal stability was evaluated up to 700 °C by DSC followed by XRD analysis at room temperature. No exothermic or endothermic peaks were detected for either sample in this temperature range, which is consistent with the presence of Al atoms in the Mo-phase after milling. Otherwise, melting of Al would be observed around 660 °C. Based on this result the decision was taken to perform annealing at temperatures of 700, 800 and 900 °C with 1 h holding. After cooling, the samples were structurally analyzed by XRD. The patterns are shown in Fig. 8.

Table 2
Characteristic values of the particle size distributions before and after mechanical alloying.

	Dp10 (μm)	Dp50 (μm)	Dp90 (μm)
Initial	11.5	72.3	309.9
50 h/150 rpm	8.0	30.2	93.9
25 h/300 rpm	3.1	15.0	85.8

Table 3
Chemical composition (wt.%) of the powder mixtures after mechanical alloying.

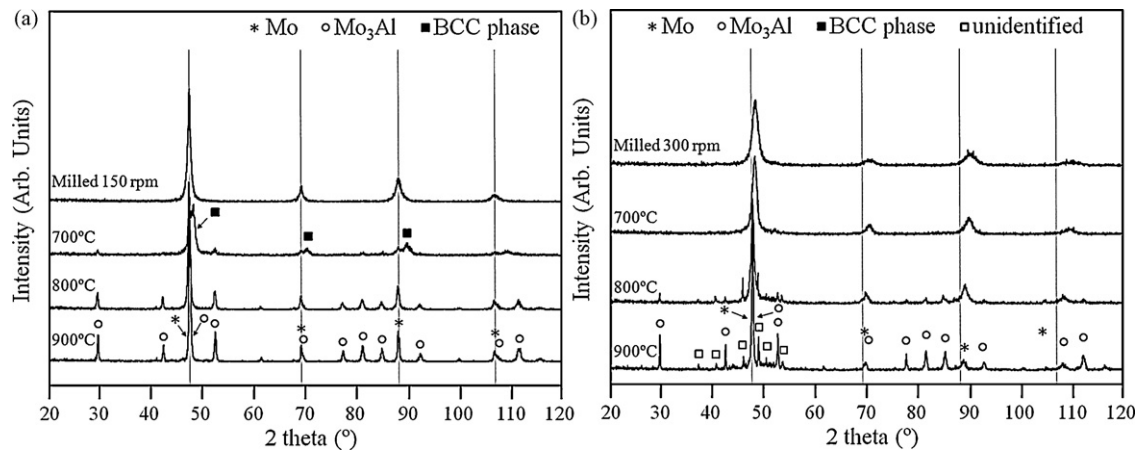|	Mo	Al	Fe	O	Mo/Al
150 rpm/100 h	82.4 ± 0.7	11.5 ± 0.3	1.6 ± 0.5	4.5 ± 0.2	7.2
300 rpm/50 h	66.2 ± 0.8	9.2 ± 0.2	20.6 ± 0.7	19.3 ± 0.3	7.2

Fig. 8. X-ray diffraction patterns of powder mixtures after MA and subsequent annealing at different temperatures. (a) 150 rpm (b) 300 rpm.
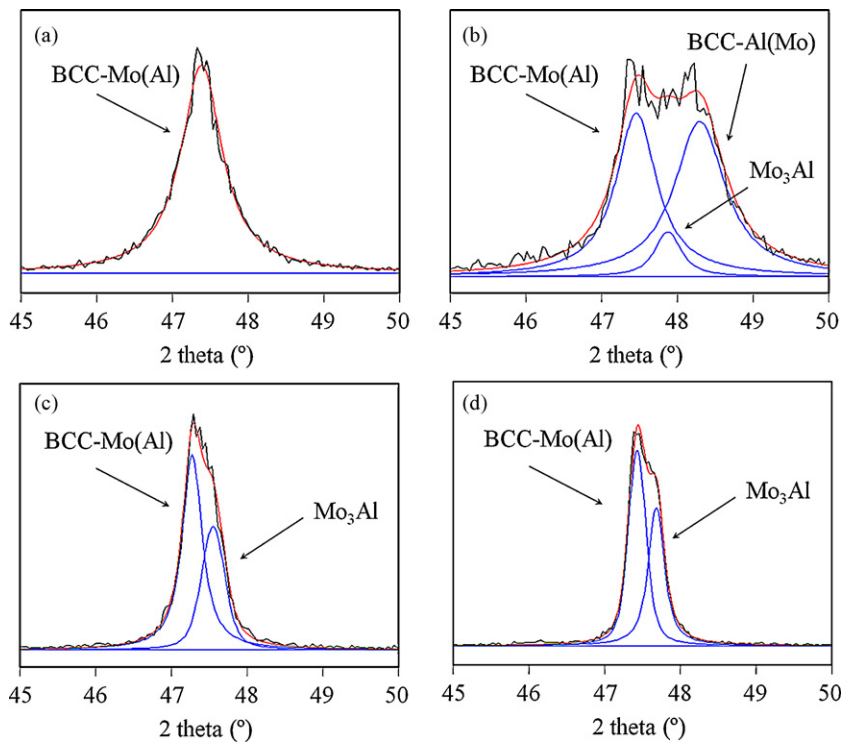

Fig. 9. Deconvolution of the XRD patterns in a 2θ range of 46–50° for the mixtures milled at 150 rpm. (a) as-milled, (b) annealed at 700 °C, (c) annealed at 800 °C and (d) annealed at 900 °C.
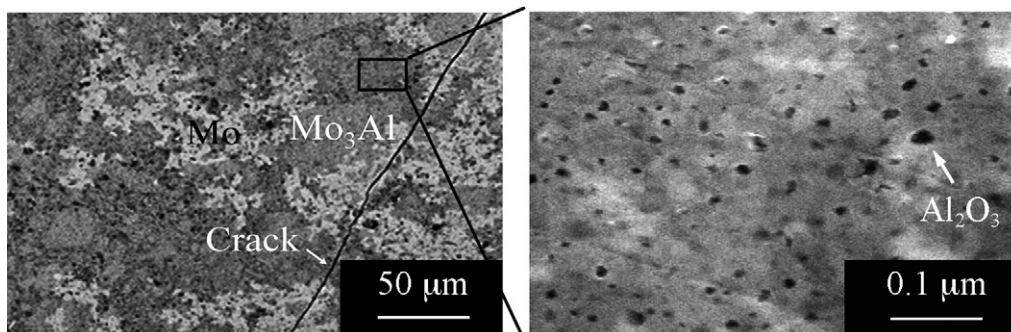

Fig. 10. BSE-SEM images of the 900 °C annealed sample milled at 150 rpm for 100 h.

The results show the formation of new structural phases in all annealed samples. Due to the superimposition of some XRD peaks, deconvolution of the spectra was performed on a 2θ range of 46–50°. Fig. 9 shows the results obtained for the mixtures milled at 150 rpm. Deconvolution of the XRD pattern of the as-milled mixture is also shown for comparison. As can be seen, after MA the experimental XRD peak corresponds to only one diffraction line, that of the BCC-Mo(Al) phase. After 700 °C annealing, there are three relatively broad peaks ascribed to three structural phases: the BCC-Mo phase existing after milling, a Mo–Al intermetallic phase and another BCC phase with a cell parameter of 3.098 Å. Due to the close proximity of the corresponding diffraction peaks it was not possible to determine whether the intermetallic phase was AlMo$_3$ or Al$_3$Mo using XRD. However, domains with an atomic chemical composition of AlMo$_3$ were detected using EPMA analysis, which makes the existence of Al$_3$Mo unlikely. The new BCC phase detected after 700 °C annealing of the mixture milled at 150 rpm for 100 h was not detected in the sample milled at 300 rpm. An additional annealing of this mixture was performed at 600 °C in order to verify if that phase could be formed at lower temperatures. However, no signs of such a phase were detected at this temperature for this sample. Probably, the explanation for this has something to do with the previously mentioned chemical composition heterogeneities found after 100 h milling at 150 rpm. It is likely that the increase in temperature induces greater long range order in the Al-rich domains that exist after milling, giving rise to a metastable BCC-Al(Mo) solid solution. The equilibrium solid solubility of molybdenum in aluminum is less than 0.07 at.% [21]. Zdujic et al. [22] studied the structural changes during mechanical alloying of Al–Mo mixtures with different chemical compositions. Their paper reports a single BCC phase for Mo contents equal to or higher than 20 at.%, indicating the possibility that the formation of a BCC aluminum-rich phase occurs in a metastable state.

For 800 and 900 °C annealings, there are only two XRD peaks in this angle range corresponding to the Mo and Mo$_3$Al intermetallic phases. No significant differences were observed between the XRD patterns of the samples annealed at these two temperatures. The amount of the Mo$_3$Al intermetallic formed during annealing increases with temperature (particularly from 700 to 800 °C), which can be seen by the increase in intensity of the XRD peaks.

For the sample milled at 300 rpm, XRD peaks of one or more additional phases are present in the XRD patterns corresponding to annealing at 800 and 900 °C. It was not possible to ascribe these peaks to a certain phase. However, taking into account that this powder mixture has a high iron content it is likely that these XRD peaks correspond to a mixed iron-based oxide or carbide phase.

No peaks of Al$_2$O$_3$ were detected in the XRD patterns of the annealed samples from either milling process (150 and 300 rpm). Nevertheless, SEM analysis showed that this phase is present in the final structures at a nanometric scale (Fig. 10). The Al$_2$O$_3$ particles are distributed uniformly. This means that crystallization of this phase did not occur during annealing. In a recent paper, Rajkovic et al. [23] studied the influence of temperature on the structure of a Cu–5 wt.% Al$_2$O$_3$ mixture obtained by mechanical alloying and subsequently hot-pressed in an argon atmosphere at 800 °C for 1 h. As in the current investigation, diffraction lines of an Al$_2$O$_3$ phase were not observed.

3.4. Determination of mechanical properties

The mechanical properties, hardness and Young's modulus, of the mechanically alloyed mixtures with and without annealing were determined by the depth-sensing indentation technique. The stress–plastic strain curves were estimated by applying reverse analysis methodology to depth-sensing indentation data, i.e. to the load vs. indentation depth curves [14,24].
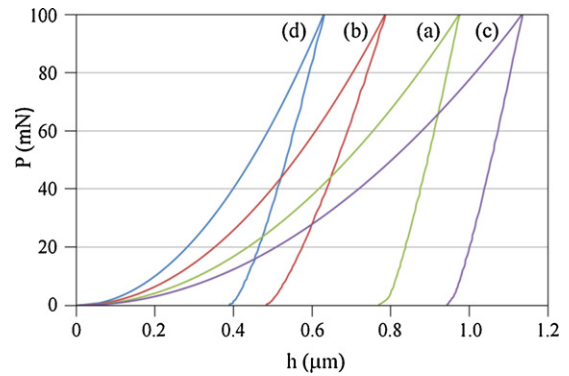

Fig. 11. Load–indentation depth curves. (a) 150 rpm/50 h; (b) 300 rpm/25 h; (c) 150 rpm/50 h annealed at 900 °C; (d) 300 rpm/25 h annealed at 900 °C.

The depth-sensing indentation tests were performed on polished samples with smooth surfaces and dense microstructures (Fig. 10). In order to obtain representative average values for the evaluated properties, 20 indentation tests were performed on different surface points of each sample. In each test, the load was increased in steps, from the first load of 0.4 mN until a nominal load of 100 mN. Sixty steps were used for both loading and unloading, with a 0.5 s delay between each step. Two creep periods of 30 s were programmed during the tests: at the maximum load, in order to stabilize the penetration depth before unloading, and at the lowest load during unloading, for thermal drift correction [25]. Fig. 11 shows examples of the load (P) vs. indentation depth (h) curves obtained for the compacts after mechanical alloying at 150 and 300 rpm with and without subsequent annealing at 900 °C. The samples are well-compacted, and this is responsible for the regular appearance of the indentation curves. Moreover, the indentation traces on the surfaces of the samples were quite regular.

The hardness, H, is defined as the maximum applied load during the indentation test, P_{max}, divided by the contact area of the indentation immediately before unloading, A_C [12]:

$$H = \frac{P_{max}}{A_C} \tag{2}$$

The following equation was used for determining the reduced Young's modulus, E_r [12]:

$$E_r = \frac{1}{2}\sqrt{\frac{\pi}{A_C}}\frac{1}{C - C_f} \tag{3}$$

where C ($C = (dh/dP)_{h_{max}}$) is the compliance of the unloading part of the indentation curve, i.e. the inverse of the stiffness, S, at the maximum load (or indentation depth): $S = 1/C = (dP/dh)_{h_{max}}$, and C_f is the frame compliance, respectively. In this equation, E_r is a function of the Young's modulus, E, and the Poisson's ratio, ν, of the specimen (s) and the indenter (i), through:

$$\frac{1}{E_r} = \frac{1 - \nu_s^2}{E_s} + \frac{1 - \nu_i^2}{E_i} \tag{4}$$

The so-called reduced elastic modulus of the material, E^*, is such that:

$$\frac{1}{E^*} = \frac{1 - \nu_s^2}{E_s} \tag{5}$$

For evaluation of the hardness (Eq. (2)) and Young's modulus (Eq. (3)) a Vickers indenter was used, and it was assumed that the contact penetration depth h_C, and consequently the contact area A_C ($A_C = 24.5 h_C^2$ in an ideal case) immediately before unloading, can be directly determined from the load–unloading curve, as follows:

$$h_C = h_{max} - \varepsilon C P_{max} \tag{6}$$

where P_{max} is the maximum load and h_{max} is the corresponding indentation depth, C is the compliance, and ε is a correction factor, which depends on the indenter geometry (for the Vickers indenter, $\varepsilon = 0.75$ was used, as usual [12])

In order to carry out the reverse analysis methodology from the depth-sensing indentation data, the stress–plastic strain curve must be expressed by an equation, such as the Swift equation, which has been used successfully in continuum plastic theory (see for example [24]):

$$\sigma = k(\varepsilon + \varepsilon_0)^n \tag{7}$$

where σ is the flow stress, ε the plastic strain, n the work-hardening coefficient, ε_0 represents a small strain value (similar to the ratio σ_y/E; $\varepsilon_0 = 0.005$, in this paper) and k a parameter such that $\sigma_y = k\varepsilon_0^n$ where σ_y is the yield stress. Therefore, the two parameters σ_y and n fully characterize the stress–plastic strain curves. The two mentioned reverse analysis approaches make use of experimental indentation results, obtained using just one indenter geometry (Vickers in this case), to estimate the representative stress, σ_r (the flow stress corresponding to a plastic strain value – representative plastic strain ε_r – in the range 3.3–4.2%, depending on the Young's modulus and representative stress values) and the work-hardening coefficient, n. Both approaches are based on the fact that materials with the same Young's modulus and representative stress exhibit similar behaviour under loading with respect to the indentation curves, whatever the value of the strain-hardening exponent, n. Moreover, the stiffness during the unloading part of the indentation curve, at the maximum load, allows n to be estimated. Finally, knowing σ_r and n allows σ_y to be derived from the Swift equation.

In the case of the reverse analysis approach proposed by Dao et al. [26], an analytical method is used to determine σ_r and n, which consists of using several dimensionless Π functions. In the present study, we used the function Π_1, for determining σ_r (corresponding to a plastic strain value ε_r of 3.3% [26]):

$$\Pi_1 = \frac{K}{\sigma_r} = -1.131\left[\ln\left(\frac{E^*}{\sigma_r}\right)\right]^3 + 13.635\left[\ln\left(\frac{E^*}{\sigma_r}\right)\right]^2$$
$$- 30.594\left[\ln\left(\frac{E^*}{\sigma_r}\right)\right] + 29.267 \tag{8}$$

where K is the curvature of the loading part of the load–indentation depth curve, in agreement with Kick's law:

$$P = Kh^2 \tag{9}$$

where P and h are the load and indentation depth, respectively. The use of this equation, for estimation of the representative stress, σ_r, presumes the previous experimental determination of the reduced elastic modulus of the material, E^* (by using Eqs. (3)–(5)), and the K parameter, which can be obtained by fitting Eq. (9) to experimental loading curves such as the ones in Fig. 10.

For estimating the work-hardening coefficient, n, the Π_2 function was then used:

$$\Pi_2 = \frac{S}{E^*h_{max}}$$
$$= (-1.40557n^3 + 0.77526n^2 + 0.15830n - 0.06831)\left[\ln\left(\frac{E^*}{\sigma_r}\right)\right]^3$$
$$+ (17.93006n^3 - 9.22091n^2 - 2.37733n + 0.86295)\left[\ln\left(\frac{E^*}{\sigma_r}\right)\right]^2 +$$
$$(-79.99715n^3 + 40.55620n^2 + 9.00157n - 2.54543)\left[\ln\left(\frac{E^*}{\sigma_r}\right)\right] +$$
$$(122.65069n^3 - 63.88418n^2 - 9.58936n + 6.20045) \tag{10}$$

where S is the stiffness of the unloading curve: $S = (dP/dh)_{h_{max}}$; h_{max} is the maximum indentation depth, i.e. at the maximum load).

Table 4
Mechanical properties of the as-milled and annealed samples, mechanically alloyed at 150 and 300 rpm.

	150 rpm		300 rpm	
	As-milled	900 °C annealing	As-milled	900 °C annealing
H (GPa)	5.7	4.2	14.0	18.4
E (GPa)	134	130	160	227
σ_y (GPa)	1.6 (1.7)	1.1 (1.1)	4.9 (σ_r = 5.0)	6.2 (σ_r = 6.3)
n	0.02 (0.01)	0.05 (0.05)	0.02	0.01

However, the use of the Π_2 function is limited when it comes to estimating a unique value for the n coefficient, namely in the case of materials for which the σ_y/E ratio becomes close to or higher than 0.03.

The reverse analysis approach proposed by Antunes et al. [14] directly compares experimental to numerical simulation indentation results, and is constructed in order to ensure unique results in all cases.

First, this reverse analysis methodology extracts the representative stress, σ_r, by comparing the loading part of the experimental and numerical indentation curves; in the current investigation, representative plastic strain values ε_r in the range 3.5–3.7% were found for the materials studied. A quasi-linear relationship between E^*/H and E^*/σ_r was observed [14], independent of the work-hardening coefficient:

$$\frac{E^*}{H} = 0.231\frac{E^*}{\sigma_r} + 4.910 \tag{11}$$

The use of this equation, to estimate the representative stress, σ_r, presumes that the hardness, H, and the reduced elastic modulus, E^*, of the material, have previously been determined by indentation test. The representative stress obtained from this equation can still be optimized by comparing the loading part of the experimental and numerical indentation curves. The value of the representative stress, in the numerical iterations, is altered until the numerical curve coincides with the experimental curve.

Second, the hardening exponent, n, is deduced from the stiffness of the unloading part of the indentation curve, S, at the maximum load, by comparing experimental and numerical values. For numerical simulation tests, the experimental reduced elastic modulus, E^*, the representative stress, σ_r, determined in the first step, and different values of work-hardening coefficient, n (Swift law), varying in a previously chosen range, are used. A linear iteration for the stiffness, S, versus the work-hardening coefficient, n, is assumed, allowing the evaluation of this coefficient.

Table 4 shows the H, E^*, σ_y and n values obtained from the compacts after mechanical alloying at 150 and 300 rpm with and without subsequent annealing at 900 °C. The σ_y and n values in parenthesis correspond to the Dao et al. reverse analysis approach [26]. For samples milled at 300 rpm, uniqueness was not obtained for the n values, using this methodology; therefore it was not possible to calculate σ_y, and instead σ_r is indicated in parenthesis.

A significant improvement in the mechanical properties was obtained for 300 rpm mechanical alloying. After milling, the hardness of the 300 rpm mixture is three times that of the 150 rpm mixture. A same trend was observed for σ_y (or σ_r). Since both mechanically alloyed mixtures were mainly composed of the BCC-Mo(Al) structure, this behaviour can only be explained by the amount of Al and impurity atoms in this phase (leading to a distortion of the BCC lattice). Moreover, as pointed out above, the existence of a BCC Al-rich phase after 150 rpm milling can also be predicted, which might also contribute to the decrease in H and σ_y values. Finally, the significant iron contamination that occurred during milling at 300 rpm may also be responsible for the improvement of the mechanical properties resulting from a solid solution

strengthening effect. With respect to the E values, a less significant increase was observed for milling at 300 rpm. This is not a surprising result since chemical bonding in both samples is predominantly metallic. The n values obtained are relatively low, meaning low plastic strain values up to the maximum load in tension.

As far as the annealed samples are concerned, a significant decrease in H and σ_y values was observed for the 150 rpm sample compared to the corresponding as-milled samples. The opposite was observed for the 300 rpm sample. Structural changes occurred with increasing temperature leading to the formation of an Mo_3Al intermetallic phase in both samples. According to the literature [27], the hardness value of this intermetallic is quite low (3.7 GPa). This fact, together with stresses released due to heating, should induce softening in both samples. However, this was not observed for the sample milled at 300 rpm. The high iron and oxygen contents present in this powder mixture might explain this result as it could lead to the formation of mixed iron-based oxide or carbide phases. In fact, as reported above, undefined diffraction peaks were detected in the XRD pattern of the 900 °C annealed sample milled at 300 rpm which might be responsible for the improvement in mechanical properties. A significant improvement in the Young's modulus was observed for this sample. Once again the formation of mixed oxides/carbides with strong covalent bonds might be responsible for the increase in E. The n value obtained for the annealed sample milled at 150 rpm is higher than that of the as-milled sample (0.05 against 0.02), indicating a slight increase in ductility. The structural changes occurring during annealing are responsible for this improvement. For 300 rpm no significant variation was noticed for the n coefficient.

4. Conclusions

Nanostructured Mo_3Al-based composites with strengthening Al_2O_3 precipitates were obtained from a $Mo_{75}Al_{25}$–15 vol.% Al_2O_3 mixture synthesized by mechanical alloying from Mo, Al and Al_2O_3 powders and subsequently annealed. It has been shown that a metastable BCC-Mo(Al) solid solution is formed during milling. With subsequent annealing at 900 °C an intermetallic Mo_3Al phase is formed from the decomposition of the supersaturated solid solution. During processing at 300 rpm there was significant contamination from the grinding media (vial and balls). This contamination was responsible for the significant improvement in the mechanical properties of the mixtures processed under these conditions. Values of H = 18.4 GPa, σ_y = 6.2 MPa and E = 227 GPa were obtained for samples milled for 50 h at 300 rpm and annealed at 900 °C. The hardening coefficient determined by reverse analysis

was 0.02 for the samples milled at 150 and 300 rpm, with and without subsequent annealing. The n values obtained for the annealed samples are relatively low, meaning low plastic strain values up to the maximum load in tension.

References

[1] H. Mecking, H. Ecking, C. Seeger, J. Phys. III 1 (6) (1991) 829–849.
[2] F. Simões, B. Trindade, Mater. Sci. Eng. A397 (2005) 257–263.
[3] M. Caetano, F.J. Oliveira, R.F. Silva, F. Simoes, B. Trindade, Rev. Adv. Mater. Sci. 2 (21) (2009) 173–182.
[4] A. Mattern, B. Huchler, D. Staudenecker, R. Oberacker, A. Nagel, M.J. Hoffmann, J. Eur. Ceram. Soc. 24 (12) (2004) 3399–3408.
[5] C.C. Koch, Mater. Sci. Eng., A 244 (1) (1998) 39–48.
[6] H. Prielipp, M. Knechtel, N. Claussen, S.K. Streiffer, H. Mullejans, M. Ruhle, J. Rodel, Mater. Sci. Eng., A 197 (1) (1995) 19–30.
[7] E. Lucchini, S. Lo Casto, O. Sbaizero, Mater. Sci. Eng. A357 (2003) 369–375.
[8] V. Udhayabanu, K.R. Ravi, V. Vinod, B.S. Murty, Intermetallics 18 (3) (2010) 353–358.
[9] S.Z. Anvari, F. Karimzadeh, M.H. Enayati, J. Alloys Compd. 477 (1–2) (2009) 178–181.
[10] K. Kawabata, E. Sato, K. Kuribayashi, Acta Mater. 50 (13) (2002) 3465–3474.
[11] M. Rafiei, M.H. Enayati, F. Karimzadeh, J. Alloys Compd. 488 (2009) 144–147.
[12] J.M. Antunes, A. Cavaleiro, L.F. Menezes, M.I. Simões, J.V. Fernandes, Surf. Coat. Technol. 149 (2002) 27–35.
[13] M. Dao, N. Chollacoop, K.J. Vliet, T.A. Venkatesh, S. Suresh, Acta Mater. 49 (2001) 3899–3918.
[14] J.M. Antunes, J.V. Fernandes, L.F. Menezes, B.M. Chaparro, Acta Mater. 55 (2007) 69–81.
[15] A.R. Yavari, P.J. Desré, T. Benameur, Phys. Rev. Lett. 68 (14) (1992) 2235.
[16] T. Benameur, A. Inoue, Mater. Trans., JIM 36 (2) (1995) 240.
[17] M. Zdujid, D. Poleti, Lj. Karanovid, K.F. Kobayashi, P.H. Shingu, Mater. Sci. Eng., A 185 (1994) 77–86.
[18] S. Enzo, R. Frattini, P. Canton, G. Mulas, P. Radaelli, Nanostruct. Mater. 12 (1–4) (1999) 547–550.
[19] J.I. Langford, J. Appl. Crystallogr. 11 (1978) 10–14.
[20] J.S. Benjamin, Metall. Trans. 1 (1970) 2943–2951.
[21] T.B. Massalski (ed.), In: "Binary Alloy Phase Diagrams", Vol. 1 (American Society for Metals, Metals Park, Ohio, 1986) p. 133.
[22] M.V. Zdujic, K.F. Kobayashi, P.H. Shingu, J. Mater. Sci. 26 (1991) 5502–5508.
[23] V. Rajkovic, D. Bozic, M.T. Jovanovic, J. Alloys Compd. 459 (2008) 177–184.
[24] J.V. Fernandes, D.M. Rodrigues, L.F. Menezes, M.F. Vieira, Int. J. Plast. 14 (1998) 537–550.
[25] M.I. Simões, J.V. Fernandes, A. Cavaleiro, Philos. Mag. A 82 (10) (2002) 1911–1919.
[26] M. Dao, N. Chollacoop, K.J. Van Vliet, T.A. Venkatesh, S. Suresh, Acta Mater. 49 (2001) 3899–3918.
[27] K.S. Kumar, in: J.H. Westtbrook, R.L. Fleischer (Eds.), Intermetallic Compounds: Principles and Practice, vol.II, John Wiley & Sons, England, 1995, pp. 252–253.